< In this revised manuscript, the changes were marked in blue. >

Impacts of Ice-Particle Size Distribution Shape Parameter on Climate Simulations with the Community Atmosphere Model Version 6 (CAM6)

Wentao Zhang[1], Xiangjun Shi[1,*], and Chunsong Lu[2]

[1] School of Atmospheric Sciences, Nanjing University of Information Science and Technology, Nanjing 210044, China.
[2] Key Laboratory for Aerosol-Cloud-Precipitation of China Meteorological Administration, Nanjing University of Information Science and Technology, Nanjing 210044, China.

Correspondence to: Xiangjun Shi (shixj@nuist.edu.cn)

Abstract. The impacts of the ice crystal size distribution shape parameter (μ_i) were considered in the two-moment bulk cloud microphysics scheme of the Community Atmosphere Model Version 6 (CAM6). The μ_i's impact on the statistical mean radii of ice crystals can be analysed based on their calculating formulas. Under the same mass (q_i) and number (N_i), the ratios of the mass-weighted radius (R_{qi}, not related to μ_i) to other statistical mean radii (e.g., effective radiative radius) are completely determined by μ_i. Off-line tests show that μ_i has a significant impact on the cloud microphysical processes owing to the μ_i-induced changes in ice crystal size distribution and statistical mean radii (excluding R_{qi}). Climate simulations show that increasing μ_i would lead to higher q_i and lower N_i in most regions, and these impacts can be explained by the changes in cloud microphysical processes. After increasing μ_i from 0 to 5, the longwave cloud radiative effect increases (stronger warming effect) by 5.58 W m^{-2} (25.11 %), and the convective precipitation rate decreases by -0.12 mm day^{-1} (7.64 %). In short, the impacts of μ_i on climate simulations are significant and the main influence mechanisms are also clear. This suggests that the μ_i-related processes deserve to be parameterized in a more realistic manner.

1 Introduction

Clouds are an integral part of the Earth's radiation budget and global water cycle (Liou, 1986; Luo and Rossow, 2004; Bony et al., 2015; Zhou et al., 2016). Since cloud microphysical processes occur at scales that are much smaller than the resolution of commonly-used atmospheric models, it remains a significant challenge for atmospheric models to represent cloud-related processes, especially ice-phase cloud microphysical processes (Mitchell et al., 2008; Spichtinger and Gierens, 2009; Wang and Penner, 2010; Erfani and Mitchell, 2016; Paukert et al., 2019; Morrison et al., 2020; Proske et al., 2021). Because it is impossible for commonly-used atmospheric models (excluding the ideal model with the recently developed Lagrangian particle-based scheme) to individually describe cloud particles (e.g., cloud droplets or ice crystals), only the macrostatistical features of cloud particles are represented in cloud microphysics schemes. From the outset, the development of cloud

microphysics schemes has resulted in two distinct categories: bulk microphysics parameterization and spectral (bin)
microphysics (Milbrandt and Yau, 2005; Khain et al., 2015). The spectral (bin) approach explicitly represents the cloud
particle size distributions (PSDs) by using tens to hundreds of bins. The computational cost of this approach is very high
because of the massive interactions among different bins. The bulk microphysics scheme represents the PSDs by a
semiempirical distribution function. Compared to the spectral (bin) scheme, the bulk microphysics scheme has high
computational efficiency and has been widely used in climate models (Morrison et al., 2005; Lohmann et al., 2007;
Salzmann et al., 2010; Gettelman and Morrison, 2015).

In the bulk cloud microphysics schemes used for climate models, the PSD is usually described by the gamma distribution
function with three parameters, namely, the intercept parameter (N_0), the slope parameter (λ), and the spectral shape
parameter (μ) (Khain et al., 2015; Morrison et al., 2020). Note that the commonly used two-moment bulk microphysics
scheme predicts only the mass and number of cloud particles, which cannot constrain these three parameters (i.e., N_0, λ, and
μ). Therefore, one of these three parameters (typically μ) must be determined from an empirical formula or set to a given
value (e.g., Morrison and Gettelman, 2008; Barahona et al., 2014; Eidhammer et al., 2017). For instance, the μ (μ_i) of ice
crystals (ICs, only represents cloud ice in this study) in the two-moment bulk stratiform cloud microphysics scheme
developed by Morrison and Gettelman 2008 (hereafter MG scheme) is set to zero (i.e., the μ_i is ignored). In recent years, off-
line tests and short-term simulations (a few days or less) with high-resolution atmospheric models (e.g., cloud-resolving
models and mesoscale models) have shown that μ_i has a significant impact on cloud microphysical processes and synoptic
systems (Milbrandt and Yau, 2005; Milbrandt and McTaggart-Cowan, 2010; Loftus et al., 2014; Khain et al., 2015;
Milbrandt et al., 2021). Unlike short-term simulations, climate simulations pay more attention to the equilibrium states or
quasi-equilibrium states because the feedback processes become important (Sherwood et al., 2015; King et al., 2020).
However, in terms of climate simulations, few studies have focused on the influence of μ_i.

In this study, in order to investigate the impacts of μ_i on climate simulations with the Community Atmosphere Model version
6 (CAM6) model, the impacts of μ_i were considered in the MG scheme by a tunable parameter. There were two major
motivations behind this work. First, are the impacts of μ_i notable? If yes, it's necessary for climate models to represent the μ_i
and μ_i-related processes in a more realistic manner. And second, what are the main mechanisms for these impacts? These
would be helpful to understand the climate simulations with the impacts of μ_i. This paper is organized as follows: the
modified MG scheme and experimental setup are described in Section 2; cloud microphysical process off-line tests and
CAM6 model simulation results are analyzed in Section 3; and finally, the summary and conclusions are provided in Section
4.

2 Model and experiments

2.1 The modified MG scheme

60 The CAM6 model, which is the atmospheric component of the Community Earth System Model Version 2.1.3 (CAM6, Bogenschutz et al., 2018; CESM2, Danabasoglu et al., 2020), was used in this study. It is noteworthy that the treatments of clouds in climate models are usually divided into two categories: convective cloud schemes with simplified cloud microphysics and larger-scale stratiform cloud schemes with relatively detailed cloud microphysics. In the CAM6 model, the convective cloud scheme does not consider the PSD of ICs (Zhang and McFarlane, 1995; Zhang et al., 1998; Bogenschutz et

65 al., 2013; Larson, 2017). The stratiform cloud microphysics was represented by the updated MG scheme with prognostic precipitation (Gettelman and Morrison, 2015). In both versions of the MG scheme, the ICs are assumed to be spherical, and the PSD of ICs is described by the gamma distribution function:

$$N'_i(D) = N_{0i} D^{\mu_i} e^{-\lambda_i D} \tag{1}$$

where $N'_i(D)$ is the number density (i.e., $\delta N_i/\delta D$) of the ICs with diameter D. N_{0i}, λ_i, and μ_i (nonnegative values) are the intercept parameter, the slope parameter, and the spectral shape parameter, respectively. Given that μ_i is known, N_{0i} and λ_i

70 can be determined by the local in-cloud IC mass and number mixing ratio (q_i and N_i, prognostic variables in units of kg kg^{-1} and kg^{-1}, respectively).

$$\lambda_i = [\frac{\pi \rho_i}{6} \frac{N_i}{q_i} \frac{\Gamma(4 + \mu_i)}{\Gamma(1 + \mu_i)}]^{1/3} \tag{2}$$

$$N_{0i} = \frac{N_i \lambda_i^{(1+\mu_i)}}{\Gamma(1 + \mu_i)} \tag{3}$$

where the IC bulk density (ρ_i) is 500 kg m^{-3} and μ_i is zero in the default MG scheme. $\Gamma(x) = \int_0^\infty t^{x-1} e^{-t} dt$ is the gamma function. It is noteworthy that the kth moment of this size distribution (M_k) is found by integrating the distribution in this form: $M_k = \int_0^\infty N_{0i} D^{\mu_i+k} e^{-\lambda_i D} dD = N_{0i} \Gamma(k + \mu_i + 1)/\lambda_i^{(k+\mu_i+1)}$ (Eidhammer et al., 2014). Furthermore, the recursive

75 property of the gamma function (i.e., $\Gamma(x + 1) = x\Gamma(x)$) is also used for the following formula derivation.

Eqs. (2), (3) also indicate that, under the same q_i and N_i, changes in μ_i could impact the other two parameters regarding the PSD of ICs (i.e., N_{0i} and λ_i). Meanwhile, the number-weighted radius (R_{ni}) related to the IC deposition/sublimation process, the effective radiative radius (R_{ei}) used for the radiative transfer scheme, and other statistical mean radii might be influenced. To better understand the influence of μ_i on the ice-phase cloud microphysical processes, the equations for calculating the

80 statistical mean radii are introduced first. The mass-weighted radius (R_{qi}) is calculated from Eq. (4). The number-weighted radius (R_{ni}), which is the so-called mathematical mean value, is calculated from Eq. (5). The area-weighted radius (R_{ai}) is calculated from Eq. (6). R_{ei}, which is defined as the cross-section weighted radius (Schumann et al., 2011; Wyser, 1998), is calculated from R_{qi}^3/R_{ai}^2 (Eq. 7). Note that R_{qi} can be calculated by q_i and N_i (the last term of Eq. 4, without μ_i), and the other

statistical mean radii (e.g., R_{ni}, R_{ai}, and R_{ei}) can be calculated by R_{qi} and μ_i (Eqs. 5-7). In other words, the ratios of the other

85   statistical mean radii (e.g., R_{ni}, R_{ai}, and R_{ei}) to R_{qi} are functions of μ_i. For nonnegative μ_i values, Eqs. (5), (6) indicate that R_{ni}

and R_{ai} are always less than R_{qi}. This can be explained by the physical reason that larger ICs contribute more to R_{qi} than to R_{ni}

and R_{ai}. Similarly, R_{ei} is always greater than R_{qi} (Eq. 7). Furthermore, Eqs. (5), (6), (7) also indicate that with increasing μ_i,

R_{ni}, R_{ai}, and R_{ei} approach R_{qi}. In Section 3.1, more analyses are provided by off-line tests.

$$R_{qi} = \frac{1}{2}\left[\frac{\int_0^\infty D^3 N_i(D)\,\mathrm{d}D}{\int_0^\infty N_i(D)\,\mathrm{d}D}\right]^{1/3} = \frac{1}{2\lambda_i}\left[\frac{\Gamma(\mu_i+4)}{\Gamma(\mu_i+1)}\right]^{1/3} = \left(\frac{3}{4\pi\rho_i}\frac{q_i}{N_i}\right)^{1/3} \tag{4}$$

$$R_{ni} = \frac{1}{2}\frac{\int_0^\infty D N_i(D)\,\mathrm{d}D}{\int_0^\infty N_i(D)\,\mathrm{d}D} = \frac{1}{2\lambda_i}\frac{\Gamma(\mu_i+2)}{\Gamma(\mu_i+1)} = R_{qi}\left[\frac{\Gamma(1+\mu_i)}{\Gamma(4+\mu_i)}\right]^{\frac{1}{3}}\frac{\Gamma(\mu_i+2)}{\Gamma(\mu_i+1)} = R_{qi}\frac{(\mu_i+1)}{[(\mu_i+3)(\mu_i+2)(\mu_i+1)]^{\frac{1}{3}}} \tag{5}$$

$$R_{ai} = \frac{1}{2}\left[\frac{\int_0^\infty D^2 N_i(D)\,\mathrm{d}D}{\int_0^\infty N_i(D)\,\mathrm{d}D}\right]^{1/2} = \frac{1}{2\lambda_i}\left[\frac{\Gamma(\mu_i+3)}{\Gamma(\mu_i+1)}\right]^{1/2} = R_{qi}\left[\frac{\Gamma(1+\mu_i)}{\Gamma(4+\mu_i)}\right]^{1/3}\left[\frac{\Gamma(\mu_i+3)}{\Gamma(\mu_i+1)}\right]^{1/2}$$

$$= R_{qi}\frac{[(\mu_i+2)(\mu_i+1)]^{\frac{1}{2}}}{[(\mu_i+3)(\mu_i+2)(\mu_i+1)]^{\frac{1}{3}}} \tag{6}$$

$$R_{ei} = \frac{1}{2}\frac{\int_0^\infty D^3 N_i(D)\,\mathrm{d}D}{\int_0^\infty D^2 N_i(D)\,\mathrm{d}D} = \frac{(R_{qi})^3}{(R_{ai})^2} = \frac{1}{2\lambda_i}\frac{\Gamma(\mu_i+4)}{\Gamma(\mu_i+3)} = R_{qi}\left[\frac{\Gamma(1+\mu_i)}{\Gamma(4+\mu_i)}\right]^{1/3}\frac{\Gamma(\mu_i+4)}{\Gamma(\mu_i+3)}$$

$$= R_{qi}\frac{(\mu_i+3)}{[(\mu_i+3)(\mu_i+2)(\mu_i+1)]^{\frac{1}{3}}} \tag{7}$$

Because μ_i is zero in the default MG scheme, the equations for the cloud microphysical processes are simplified by omitting

90   μ_i (Morrison and Gettelman, 2008; Gettelman and Morrison, 2015). In this study, these equations are modified to consider

the impact of μ_i (i.e., nonzero μ_i). In the default MG scheme, there are three cloud microphysical processes, which are related

to the PSD of ICs. They consist of the deposition/sublimation of ICs, the autoconversion of IC to snow, and the mass-

weighted and number-weighted IC fall velocities (V_{qi} and V_{ni}), respectively. Table 1 shows the original and modified

equations for these cloud microphysical processes. The dq_i/dt (i.e., the time derivative of q_i) caused by the

95   deposition/sublimation process (including the Wegener-Bergeron process in mixed-phase clouds) is calculated from $dq_i/dt =$

$S_i/(T_p\tau_i)$, where S_i, T_p, and τ_i are the ice supersaturation, a psychrometric correction to account for the release of latent heat,

and the supersaturation relaxation time scale, respectively (Morrison and Gettelman, 2008). Among them, τ_i is related to μ_i.

In the original equation of τ_i (Table 1, left column), $N_{0i} = \lambda_i N_i$ (Eq. 3) and $\lambda_i^{-1} = 2R_{ni}$ at $\mu_i = 0$ (Eq. 5). Therefore, the original

equation for τ_i can be rewritten as the modified equation (Table 1, right column). The modified equation indicates that τ_i is

100   inversely proportional to $N_i R_{ni}$, which is consistent with the equation obtained by Korolev et al. (2003). This modified

equation also indicates that, under the same q_i and N_i (R_{qi} is also fixed), μ_i can affect τ_i (i.e., the IC deposition/sublimation process) via the influence on R_{ni}. In the MG scheme, ICs with radii greater than the threshold (R_{cs}) are considered to be snow. Correspondingly, the mass and number of ICs converted to snow (q_{iauto} and N_{iauto}) are represented by the integration of those ICs with radii greater than R_{cs}. Therefore, the incomplete gamma function, ($\Gamma(s,x) = \int_x^\infty t^{s-1}e^{-t}\,dt$), is used to calculate

105   q_{iauto} and N_{iauto} (right column). It is necessary to note that, at $\mu_i = 0$, the modified equations for q_{iauto} and N_{iauto} can be rewritten as the original equations (i.e., omitting μ_i, left column) based on a property of the incomplete gamma function (i.e., $\Gamma(s,x) = (s-1)!\,e^{-x}\sum_{k=0}^{s-1}\frac{x^k}{k!}$, where s is a positive integer). Based on the diameter-fall speed relationship, $V = aD^b$ (a and b are empirical coefficients), and the properties of the gamma function, μ_i is considered in the equations for mass-weighted and number-weighted terminal fall speeds (V_{qi} and V_{ni}, Table 1).

110   **Table 1.** Equations for calculating the μ_i-related cloud microphysical processes*.

	Original ($\mu_i = 0$)	Modification (nonzero μ_i)
τ_i	$\dfrac{1}{2\pi\rho_a D_v N_{0i}\lambda_i^{-2}}$	$\dfrac{1}{2\pi\rho_a D_v N_i 2R_{ni}}$
N_{iauto}	$\dfrac{N_{0i}}{\lambda_i}e^{-\lambda_i 2R_{cs}}$	$N_{0i}\dfrac{\Gamma(1+\mu_i,\lambda_i 2R_{cs})}{\lambda_i^{1+\mu_i}}$
q_{iauto}	$\dfrac{\pi\rho_i N_{0i}}{6}\left[\dfrac{(2R_{cs})^3}{\lambda_i}+\dfrac{3(2R_{cs})^2}{\lambda_i^2}+\dfrac{6(2R_{cs})}{\lambda_i^3}+\dfrac{6}{\lambda_i^4}\right]e^{-\lambda_i 2R_{cs}}$	$\dfrac{\pi\rho_i N_{0i}}{6}\dfrac{\Gamma(4+\mu_i,\lambda_i 2R_{cs})}{\lambda_i^{4+\mu_i}}$
V_{ni}	$\dfrac{(\frac{\rho_{a850}}{\rho_a})^{0.35}a\Gamma(1+b)}{\lambda_i^b\Gamma(1)}$	$\dfrac{(\frac{\rho_{a850}}{\rho_a})^{0.35}a\Gamma(1+b+\mu_i)}{\lambda_i^b\Gamma(1+\mu_i)}$
V_{qi}	$\dfrac{(\frac{\rho_{a850}}{\rho_a})^{0.35}a\Gamma(4+b)}{\lambda_i^b\Gamma(4)}$	$\dfrac{(\frac{\rho_{a850}}{\rho_a})^{0.35}a\Gamma(4+b+\mu_i)}{\lambda_i^b\Gamma(4+\mu_i)}$

*Where D_v is the diffusivity of water vapor in air (D_v is calculated as a function of temperature and pressure, $D_v = 8.794\times10^{-5}\times T^{1.81}/P$); R_{cs} is the threshold radius for the autoconversion of IC to snow ($R_{cs} = 100$ μm); ρ_a is the air density; ρ_{a850} is the reference air density at 850 hPa, and a and b are empirical coefficients ($a = 700$ m^{1-b} s^{-1}, $b = 1$).

2.2 CAM6 experimental design

115   Observational studies have shown that μ_i is less than 5 under most conditions (Heymsfield, 2003; McFarquhar et al., 2015). This study focuses only on investigating the influence of μ_i. There are four μ_i-related processes (i.e., the radiative transfer process and three cloud microphysical processes) in the modified CAM6 model. Note that μ_i can be set to different values for different processes with the advantage of model simulations. Seven experiments were conducted in this study (Table 2). The

Mu0 experiment is considered to be the reference experiment because μ_i is set to zero for all of the μ_i-related processes. The μ_i is set to 2 for all of the μ_i-related processes in the Mu2 experiment, and the μ_i is set to 5 for all of the μ_i-related processes in the Mu5 experiment. The comparison between the Mu2 (or Mu5) and Mu0 experiments shows the influence of μ_i on climate simulations. Furthermore, to investigate the influence of each μ_i-related process, an additional four experiments, namely, Tao5, Auto5, Fall5, and Rei5, were conducted. It is also necessary to investigate negative μ_i because negative μ_i has also been reported by observational studies. However, the bulk cloud microphysics schemes usually constrain μ_i to be nonnegative (see Appendix A). Therefore, only nonnegative μ_i was investigated. In this study, for ease of expression, "Δ" is used to denote the difference from the Mu0 experiment (e.g., ΔTao5 = Tao5 − Mu0). Without specification, the comparisons between model simulations are relative to the Mu0 experiment. When analyzing a cloud property variable (e.g., q_i), it is necessary to know which experiment the variable comes from. To show this information, the experiment name is added as a superscript. For example, the q_i from the Mu5 experiment is denoted as q_i^{Mu5}, the difference in q_i between the Mu5 and Mu0 experiments is denoted as $q_i^{\Delta Mu5}$, and the relative change of q_i from the Mu5 experiment is denoted as $q_i^{\Delta Mu5/Mu0}$.

In this study, all experiments were atmosphere-only simulations (i.e., sea surface temperature and sea ice are prescribed) with a horizontal resolution of 1.9° latitude × 2.5° longitude and 32 vertical layers. All experiments run for 11 model years and the last 10 years were used for the analyses. In addition, the standard deviation calculated from the averages of each year (i.e., 10 averages) was used to check the statistical significance of the multiyear average (i.e., 10-year average).

Table 2. The values of μ_i in all experiments conducted in this study. μ_{i_tao}, μ_{i_auto}, μ_{i_fall}, and μ_{i_rei} indicate the μ_i used for calculating the IC deposition/sublimation (*tao*), autoconversion of IC to snow (*auto*), IC fall velocity (*fall*), and the R_{ei} used for the radiation scheme (*rei*), respectively.
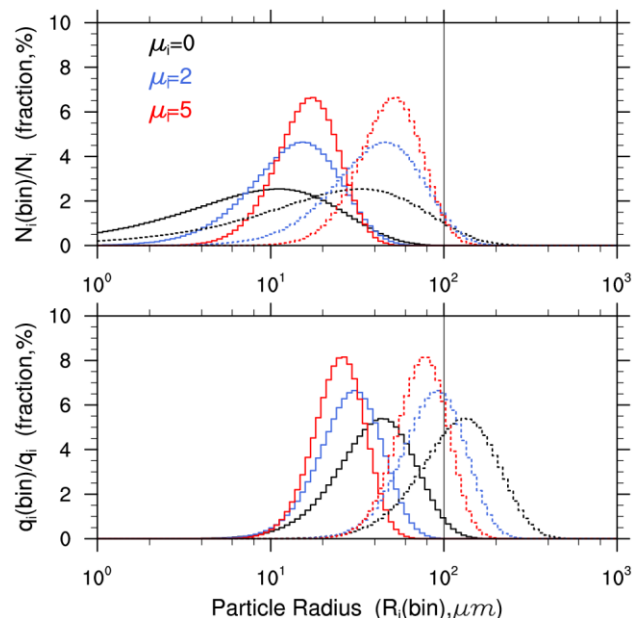
Names	μ_{i_tao}	μ_{i_auto}	μ_{i_fall}	μ_{i_rei}
Mu0	0	0	0	0
Mu2	2	2	2	2
Mu5	5	5	5	5
Tao5	5	0	0	0
Auto5	0	5	0	0
Fall5	0	0	5	0
Rei5	0	0	0	5

3 Results and analysis

3.1 Off-line tests

140 To better understand the impact of μ_i on climate simulations, the impacts of μ_i on the IC PSD and μ_i-related cloud microphysical processes are first illustrated by off-line tests. In these off-line tests, the impact of μ_i was analyzed at a given R_{qi} (i.e., the ratio of q_i to N_i is fixed).

Eqs. (1), (2), (3) indicate that the normalized IC size distribution (i.e., the relative contributions of each bin) can be calculated from R_{qi} and μ_i. Fig. 1 shows the impact of μ_i on the normalized PSDs of ICs. Under the same μ_i, the shapes of the

145 PSDs (i.e., the relative number or mass contributions of each bin) with $R_{qi} = 20$ μm (small IC scenario) are the same as those with $R_{qi} = 60$ μm (large IC scenario). In other words, the shape of the PSD is completely determined by μ_i (i.e., spectral shape parameter). As expected, the PSDs move toward larger radii with increasing R_{qi}. As introduced in the study of Milbrandt et al. (2021), the PSD becomes narrow with increasing μ_i. Note that, in terms of number, the contributions of the smaller size bins significantly decrease with increasing μ_i. Unlike the number contributions, the mass contributions of the

150 larger size bins significantly decrease with increasing μ_i because the mass contribution is more sensitive to the IC radius. Under the large IC scenario (i.e., $R_{qi} = 60$ μm), the mass contribution of the ICs with radii greater than R_{cs} is significantly decreased with increasing μ_i. The above analyses suggest that the cloud microphysical processes that depend on the PSD of ICs (e.g., autoconversion of IC to snow) might be significantly influenced by μ_i.

155 **Figure 1.** The relative number (upper panel) and mass (lower panel) contributions from each radius bin of ICs. Each bin width is the same based on the logarithm of the particle radius. N_i and q_i are the total number and mass of ICs, respectively. A total of 100 bins were used

here. The solid lines indicate the normal IC scenario (i.e., $R_{qi} = 20$ µm), and the dotted lines indicate the large IC scenario (i.e., $R_{qi} = 60$ µm). The vertical black line indicates the R_{cs} that was used for the autoconversion of IC to snow ($R_{cs} = 100$ µm).

The off-line tests were performed for the μ_i-related cloud microphysical processes and statistical mean radii (Table 3). As introduced in Section 2.1, R_{ni}, R_{ai}, and R_{ei} can be calculated from R_{qi} and μ_i. Both R_{ni} and R_{ai} significantly increase with increasing μ_i (Table 3). This is in agreement with their calculation equations (Eqs. 5, 6). R_{ni} is approximately half of R_{qi} at $\mu_i = 0$ (i.e., 11.00/20 and 33.02/60), while R_{ni} is close to R_{qi} at $\mu_i = 5$ (i.e., 17.26/20 and 51.78/60). According to the calculation equation of R_{ei} (Eq. 7), R_{ei} decreases with increasing μ_i. The ratios of R_{ei} to R_{qi} at $\mu_i = 0$, 2, and 5 are 1.65 (i.e., 33.02/20 and 99.06/60), 1.28 (i.e., 25.54/20 and 76.63/60), and 1.15 (i.e., 23.01/20 and 69.04/60), respectively. It is necessary to point out that with increasing μ_i, both R_{ni}, R_{ai}, and R_{ei} approach R_{qi} (Table 3) because the PSD of ICs becomes narrow (Fig.1). As expected, τ_i decreases with increasing μ_i (Table 3) because τ_i is inversely proportional to R_{ni} (Table 2). The decrease in τ_i suggests that the dq_i/dt caused by the deposition/sublimation process is accelerated (Morrison and Gettelman, 2008). Compared to the $1/\tau_i$ with $\mu_i = 0$ (i.e., 3.35×10^{-4} s^{-1} and 10.04×10^{-4} s^{-1}), the $1/\tau_i$ with $\mu_i = 2$ (4.66×10^{-4} s^{-1} and 13.98×10^{-4} s^{-1}) and $\mu_i = 5$ (5.25×10^{-4} s^{-1} and 15.74×10^{-4} s^{-1}) increase by 39.10 % and 56.72 %, respectively. This is consistent with the previous finding (ICs vapor deposition process is obviously accelerated by increasing μ_i) reported by Mitchell (1991). In Table 3, N_{iauto}/N_i and q_{iauto}/q_i indicate the portion of ICs that convert to snow in terms of number and mass, respectively. Under the small IC scenario (i.e., $R_{qi} = 20$ µm), regardless of the value of μ_i, both N_{iauto}/N_i and q_{iauto}/q_i are very small (< 2 %, Table 3) because there are few ICs with radii greater than R_{cs} (Fig. 1). Under the large IC scenario (i.e., $R_{qi} = 60$ µm), there is a considerable portion of ICs with radii greater than R_{cs}, especially the mass contribution (Fig. 1). The q_{iauto}/q_i at $\mu_i = 0$, 2, and 5 are 64.08 %, 36.54 %, and 18.40 %, respectively (Table 3). This suggests that the autoconversion of IC to snow becomes difficult with increasing μ_i. Compared with the considerable values for q_{iauto}/q_i, the N_{iauto}/N_i is relatively small (i.e., 4.84 % at $\mu_i = 0$, 4.23 % at $\mu_i = 2$, and 2.63 % at $\mu_i = 5$). Therefore, the R_{qi} of the residual ICs ($R_{qi\_afterauto}$; 43.36 µm at $\mu_i = 0$, 52.31 µm at $\mu_i = 2$, and 56.57 µm at $\mu_i = 5$) is obviously lower than the original R_{qi} (60 µm). During the falling process, it is inevitable that V_{qi} is greater than V_{ni} because larger ICs with faster falling contribute more in the V_{qi}. Thus, larger ICs appear preferentially in the lower model layers. This is called the size-sorting mechanism (Milbrandt and Yau, 2005). V_{qi} decreases with increasing μ_i, while V_{ni} increases with increasing μ_i (Table 3). This could also be explained by their calculation equations (the corresponding derivations are similar to those for R_{ni}, R_{ai}, and R_{ei}, not shown). With increasing μ_i, the difference between V_{qi} and V_{ni} decreases (Table 3) because the PSD of ICs becomes narrow (Fig.1). As a result, the size-sorting process becomes slow. For instance, there are many ICs with $R_{qi} = 60$ µm in a model layer. The height of each model layer is 200 m. After one model time step (10 min), some ICs fall into the lower layer. For $\mu_i = 0$, the R_{qi} of the ICs that are still in the model layer ($R_{qi\_leftover}$) is 42.11 µm, and the R_{qi} of the ICs in the lower layer ($R_{qi\_lowlayer}$) is 95.24 µm. For $\mu_i = 2$, $R_{qi\_leftover}$ is 52.45 µm, and $R_{qi\_lowerlayer}$ is 75.60 µm. For $\mu_i = 5$, $R_{qi\_leftover}$ is 55.81 µm, and $R_{qi\_lowerlayer}$ is 68.68 µm. It is clear that the difference in R_{qi} between these two adjacent layers that is caused by the sedimentation process (i.e., the difference

between $R_{qi\_leftover}$ and $R_{qi\_lowerlayer}$) becomes small with increasing μ_i. In short, the above analyses clearly suggest that μ_i has a significant impact on the cloud microphysical processes and statistical mean radii of ICs.

Table 3. Off-line tests* for the cloud microphysical processes and statistical mean radii at $R_{qi} = 20\ \mu m$ (left) and $R_{qi} = 60\ \mu m$ (right).

	$R_{qi} = 20\ \mu m$			$R_{qi} = 60\ \mu m$		
	$\mu_i = 0$	$\mu_i = 2$	$\mu_i = 5$	$\mu_i = 0$	$\mu_i = 2$	$\mu_i = 5$
R_{ni} (μm)	11.00	15.33	17.26	33.02	45.98	51.78
R_{ai} (μm)	15.57	17.70	18.64	46.70	53.09	55.93
R_{ei} (μm)	33.02	25.54	23.01	99.06	76.63	69.04
$1/\tau_i$ (10^{-4} s^{-1})	3.35	4.66	5.25	10.04	13.98	15.74
τ_i (s)	2989.21	2146.68	1906.05	996.40	715.56	635.35
q_{iauto}/q_i (%)	2.00	0.01	0	64.08	36.54	18.40
N_{iauto}/N_i (%)	0.01	0	0	4.84	4.23	2.63
$R_{qi\_afterauto}$ (μm)	19.87	20.00	20.00	43.36	52.31	56.57
V_{qi} (cm s^{-1})	7.96	5.54	4.68	23.87	16.62	14.04
V_{ni} (cm s^{-1})	1.99	2.77	3.12	5.97	8.31	9.36

*Note τ_i is calculated at $T = 220$ K, $P = 330$ hPa, and $N_i = 10^5$ kg^{-1} (~50 L^{-1}). V_{ni} and V_{qi} are calculated at $T = 220$ K and $P = 330$ hPa.

3.2 CAM6 simulations

During the evolution of stratiform clouds, the properties of ice clouds (e.g., q_i, N_i, and R_{ni}, including mixed-phase clouds) largely determine the ice-phase cloud microphysical processes. Meanwhile, these cloud microphysical processes in turn change the cloud properties. They interact as both cause and effect and finally reach equilibrium climate states. To facilitate the subsequent analyses, the cloud properties and μ_i-related cloud microphysical processes are shown together in one figure. For ease of expression, "δ" is used to denote the changes in cloud properties that are caused by the cloud microphysical process during one model time step (tendency $\times$ one time step). For example, the changes in q_i and N_i that are caused by the sedimentation process during one model time step are denoted as δq_{ised} and δN_{ised}, respectively.
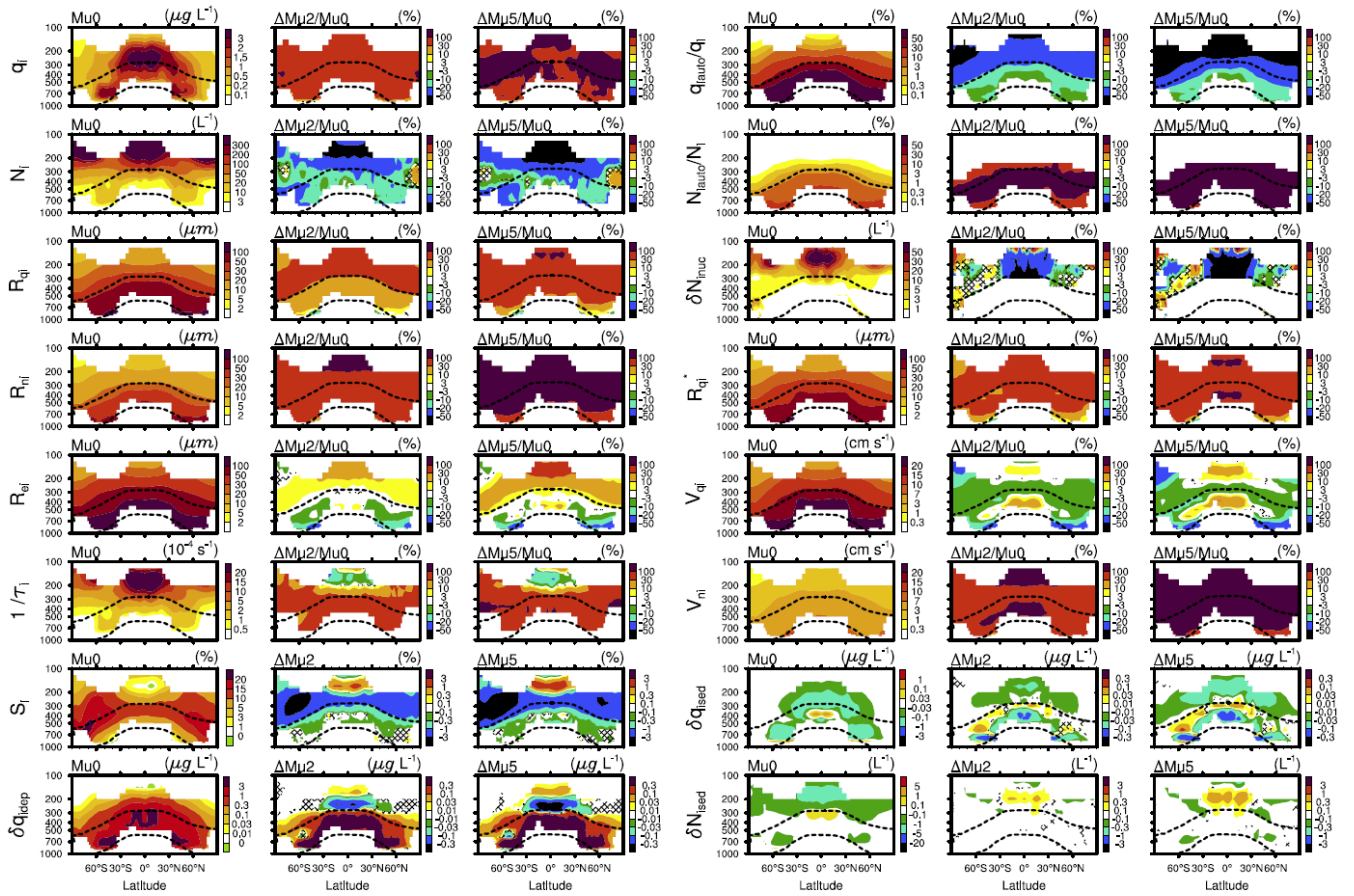
Figure 2. Annual zonal mean in-cloud variables from the Mu0 (first and fourth columns), ΔMu2 (second and fifth columns) and ΔMu5 (third and sixth columns) experiments. Shown are the ICs mass mixing ratio (q_i) and number density (N_i), mass-weighted and number-weighted radii (R_{qi} and R_{ni}), effective radius (R_{ei}), reciprocal of the supersaturation relaxation time scale ($1/\tau_i$), ice supersaturation (S_i), change in q_i caused by deposition/sublimation process (δq_{idep}), portion of ICs that are converted to snow in terms of mass and number (q_{iauto}/q_i and N_{iauto}/N_i), newly formed IC number density from the nucleation process (δN_{inuc}), the updated mass-weighted radius (R_{qi}^*) used for calculating the sedimentation process, mass-weighted and number-weighted fall velocities (V_{qi} and V_{ni}), and changes in q_i and N_i that are caused by the sedimentation process (δq_{ised} and δN_{ised}). Except for δq_{idep}, δq_{ised}, δN_{inuc} and δN_{ised}, the other variables are shown as their relative changes (i.e., ΔMu2/Mu0 and ΔMu5/Mu0). The Y-axis indicates the atmospheric pressure (unit: hPa). The two black dashed curves are the 0 and −37 °C isotherms. All results are sampled from model grids where the ice cloud fraction is greater than 1 %. The shadows indicate that the differences between two experiments are not significant at the 95 % level based on the Student's t test.

Fig. 2 shows the model results from the Mu0, Mu2, and Mu5 experiments. The q_i^{Mu0} is larger in the upper tropical troposphere (> 3 μg L^{-1}) and relatively larger in the lower troposphere over middle latitudes in both hemispheres (> 1 μg L^{-1}). The spatial pattern of q_i^{Mu0} is generally in agreement with the satellite retrieval data (Li et al., 2012). Higher N_i^{Mu0} (> 200 L^{-1}) can be found in the tropopause region, where homogeneous freezing produces a large number of ICs (not shown) due to sufficient soluble aerosol particles, higher subgrid vertical velocity and lower temperature (Shi et al., 2015). All statistical

mean radii (i.e., R_{qi}, R_{ni}, and R_{ei}) decrease with altitude increasing. One possible reason is that it is hard for ICs to grow big in the upper troposphere because the water vapor density is very small over there (lower temperature). Furthermore, the size-sorting effect (i.e., sedimentation process) could also be a contributor to this phenomenon (Milbrandt and Yau, 2005; Khain et al., 2015). As expected, R_{ni} is less than R_{qi}, and R_{ei} is larger than R_{qi}. After considering the impact of μ_i (i.e., $\mu_i = 2$ or 5), the ΔMu2 and ΔMu5 experiments show that q_i is significantly increased while N_i is significantly decreased. The $q_i^{\Delta Mu2/Mu0}$ is 30-100 % in nearly all regions, and the $q_i^{\Delta Mu5/Mu0}$ reaches even higher levels (> 100 %) in most regions. Both $N_i^{\Delta Mu2/Mu0}$ and $N_i^{\Delta Mu5/Mu0}$ are < −20 % above the −37 °C isotherm and even reach −50 % in the upper tropical troposphere. Consistent with the increase in q_i and the decrease in N_i, the R_{qi} significantly increases. The $R_{qi}^{\Delta Mu2/Mu0}$ is 30-100 % above the −37 °C isotherm, and the $R_{qi}^{\Delta Mu5/Mu0}$ is 30-100 % in most regions and even reaches 100 % in a few regions of the upper tropical troposphere. Because R_{ni} increases with increasing μ_i at a fixed R_{qi} value (Section 3.1), the relative increases in R_{ni} from the ΔMu2 and ΔMu5 experiments (i.e., $R_{ni}^{\Delta Mu2/Mu0}$ and $R_{ni}^{\Delta Mu5/Mu0}$) are obviously higher than the relative increases in R_{qi} (i.e., $R_{qi}^{\Delta Mu2/Mu0}$ and $R_{qi}^{\Delta Mu5/Mu0}$). The $R_{ni}^{\Delta Mu2/Mu0}$ is > 100 % in some regions, and the $R_{ni}^{\Delta Mu5/Mu0}$ is > 100 % in most regions. Compared with the relative increases in R_{qi}, the relative increases in R_{ei} from the ΔMu2 and ΔMu5 experiments are obviously reduced or even negative because R_{ei} decreases with increasing μ_i at a fixed R_{qi} value (Section 3.1). Overall, the impacts of μ_i on q_i and N_i are notable. The changes in the statistical mean radii (i.e., R_{qi}, R_{ni}, and R_{ei}) can be explained by the changes in q_i, N_i, and μ_i.

This paragraph analyzes the interaction between the ice cloud properties (q_i , N_i, and R_{ni}) and the IC deposition/sublimation process, and the influence of μ_i on this interaction. Since $1/\tau_i$ is proportional to $N_i R_{ni}$ (Table 1), the $1/\tau_i^{Mu0}$ is larger in the upper tropical troposphere (> 20×10^{-4} s^{-1}) due to the high N_i^{Mu0} (> 200 L^{-1}). Both the ΔMu2 and ΔMu5 experiments show that the $1/\tau_i$ increases in most regions because the relative increase in R_{ni} (i.e., $R_{ni}^{\Delta Mu2/Mu0}$ and $R_{ni}^{\Delta Mu5/Mu0}$) is stronger than the relative decrease in N_i (i.e., $N_i^{\Delta Mu2/Mu0}$ and $N_i^{\Delta Mu5/Mu0}$). However, the $1/\tau_i$ is slightly decreased in some regions of the upper tropical troposphere because the relative decrease in N_i is remarkable (< −50 %) in these regions. The δq_{idep} which indicates the change in q_i caused by the deposition/sublimation process is mainly determined by the $1/\tau_i$ and in-cloud ice supersaturation (S_i) (Morrison and Gettelman, 2008). Except for a very small region, the annual zonal mean S_i^{Mu0} is positive. This is consistent with the deposition events being much more frequent than sublimation events (not shown). When $S_i > 0$, ice-supersaturation (i.e., $S_i > 0$) towards ice-saturation (i.e., $S_i = 0$) occurs because the water vapor is consumed by δq_{idep} (Korolev et al., 2003; Krämer et al., 2009). The S_i^{Mu0} is lower (< 3 %) in the upper tropical troposphere due to the high $1/\tau_i^{Mu0}$ (> 20×10^{-4} s^{-1}). Both the ΔMu2 and ΔMu5 experiments show that S_i is increased in the upper tropical troposphere due to the decreasing $1/\tau_i$, and S_i is decreased in the other regions due to the increasing $1/\tau_i$. It is noteworthy that the $S_i^{\Delta Mu2}$ and $S_i^{\Delta Mu5}$ in the mixed-phase cloud layers are obviously weaker than those in the pure ice cloud layers (i.e., above the −37 °C isotherm). This is consistent with that the S_i is relatively stable in mixed-phase clouds because liquid droplets are often present. The δq_{idep}^{Mu0} is generally decreased with the altitude because the saturated vapor pressure significantly decreases with decreasing air temperature. The comparison between δq_{idep} and q_i suggests that δq_{idep} is an important source of q_i. The $\delta q_{idep}^{\Delta Mu2}$ and $\delta q_{idep}^{\Delta Mu5}$ are greater than 0.1 μg L^{-1} in most mixed-phase cloud layers due to the strongly increasing $1/\tau_i$ and

relatively stable S_i values. This suggests that the increasing μ_i could lead to a higher equilibrium state of q_i in the mixed-phase cloud layers via the deposition process. The $\delta q_{idep}^{\Delta Mu2}$ and $\delta q_{idep}^{\Delta Mu5}$ are negative between 200 hPa and 300 hPa mainly because the $S_i^{\Delta Mu2}$ and $S_i^{\Delta Mu5}$ are negative and the $1/\tau_i^{\Delta Mu2/Mu0}$ and $1/\tau_i^{\Delta Mu5/Mu0}$ are relatively small. The $\delta q_{idep}^{\Delta Mu2}$ and $\delta q_{idep}^{\Delta Mu5}$ are positive above 100 hPa mainly because the $S_i^{\Delta Mu2}$ and $S_i^{\Delta Mu5}$ are positive. These results indicate that the impact of μ_i on δq_{idep} becomes complex above the $-37\ °C$ isotherm, where S_i is more susceptible to $1/\tau_i$ and δq_{idep}. Meanwhile, the impact of μ_i on δq_{idep} also becomes weak above the $-37\ °C$ isotherm because the feedback processes (i.e., the interaction between S_i and δq_{idep}) become important. In short, the μ_i-induced changes in the deposition/sublimation process (i.e., $1/\tau_i$ and δq_{idep}) can be largely explained by the changes in N_i and R_{ni}. One reason for the higher q_i in the mixed-phase cloud layers from the Mu2 and Mu5 experiments is that δq_{idep} increases with increasing μ_i.

This paragraph analyzes the interaction between the ice cloud properties (q_i, N_i, and R_{qi}) and the autoconversion of IC to snow process (hereafter the autoconversion process), and the influence of μ_i on this interaction. Both q_{iauto}/q_i^{Mu0} and N_{iauto}/N_i^{Mu0} are decreased with the altitude because the R_{qi}^{Mu0} is decreased with the altitude. As expected, the q_{iauto}/q_i^{Mu0} is considerable and much larger than the N_{iauto}/N_i^{Mu0}. It is clear that the autoconversion process is an important sink of q_i. However, the autoconversion process is not an important sink of N_i because the N_{iauto}/N_i is very small. Both the $\Delta Mu2$ and $\Delta Mu5$ experiments show that the q_{iauto}/q_i is significantly decreased because the autoconversion process obviously becomes difficult at higher μ_i values (off-line tests, Section 3.1). The difficult autoconversion process leads to an equilibrium state with higher q_i and larger R_{qi}. Because of the larger R_{qi}, the N_{iauto}/N_i from the Mu2 and Mu5 experiments are significantly increased. The increasing N_{iauto}/N_i from the Mu2 and Mu5 experiments might be a main reason for the decrease in N_i in the mixed-phase cloud layers. However, the remarkable decrease in N_i (mostly in the pure ice cloud layers) from the Mu2 and Mu5 experiments is mainly due to the ice nucleation process. In the MG scheme, the newly formed IC number density (excluding the ICs in mixed-phase clouds) is calculated by a physically based ice nucleation parameterization (Liu and Penner, 2005). Because the autoconversion process becomes difficult in the Mu2 and Mu5 experiments, the in-cloud ICs should have longer lifetimes and larger radii. As a result, δN_{inuc}, which denotes the newly formed IC number density from the nucleation process, significantly decreases in the Mu2 and Mu5 experiments (Fig. 2). The main reason is that the pre-existing ICs would hinder the subsequent ice nucleation process (especially for homogeneous freezing) owing to the depletion of water vapor via deposition growth (Barahona et al., 2014; Shi et al., 2015). δN_{inuc} is the main source of N_i. Therefore, both the $\Delta Mu2$ and $\Delta Mu5$ experiments show that N_i is significantly decreased. In short, the increase in μ_i causes the autoconversion process to be difficult and then leads to a higher equilibrium state of q_i and R_{qi}. Meanwhile, N_i is significantly decreased due to the higher equilibrium state of q_i and R_{qi} (i.e., the stronger suppression effect of the pre-existing ICs on the ice nucleation process).

This paragraph analyzes the interaction between the ice cloud properties and the IC sedimentation process, and the influence of μ_i on this interaction. The sedimentation process is the last cloud microphysical process in the MG scheme. The IC fall velocity is calculated based on the updated cloud properties (i.e., the other cloud microphysical processes at this model time step have been considered). Here, R_{qi}^{*} denotes the updated R_{qi}, which includes the changes caused by the

deposition/sublimation and autoconversion processes at this model time step. In the mixed-phase cloud layers, the $R_{qi}^{*,\text{Mu0}}$ is slightly less than the R_{qi}^{Mu0} because the sedimentation process has not occurred. After considering the impacts of μ_i on the cloud microphysical processes introduced above, the relative increases in R_{qi}^* from the ΔMu2 and ΔMu5 experiments (i.e., $R_{qi}^{*,\Delta\text{Mu2/Mu0}}$ and $R_{qi}^{*,\Delta\text{Mu5/Mu0}}$) are higher than the relative increase in R_{qi}. As expected, both V_{qi}^{Mu0} and V_{ni}^{Mu0} decrease with

290   altitude increasing, and the V_{qi}^{Mu0} is obviously larger than the V_{ni}^{Mu0}. Although the $R_{qi}^{*,\Delta\text{Mu2/Mu0}}$ and $R_{qi}^{*,\Delta\text{Mu5/Mu0}}$ are positive, the $V_{qi}^{\Delta\text{Mu2/Mu0}}$ and $V_{qi}^{\Delta\text{Mu5/Mu0}}$ are negative in most regions because V_{qi} decreases with increasing μ_i (off-line tests, Section 3.1). However, both $V_{qi}^{\Delta\text{Mu2/Mu0}}$ and $V_{qi}^{\Delta\text{Mu5/Mu0}}$ are positive in some layers over the tropics and subtropics, where the $R_{qi}^{*,\Delta\text{Mu2/Mu0}}$ and $R_{qi}^{*,\Delta\text{Mu5/Mu0}}$ are relatively higher. Because V_{ni} increases with increasing μ_i at a fixed R_{qi} value (off-line tests, Table 3) and the R_{qi}^* from the Mu2 and Mu5 experiments are increased, the relative increases in V_{ni} from the ΔMu2 and

295   ΔMu5 experiments are remarkable. The $V_{ni}^{\Delta\text{Mu2/Mu0}}$ is $> 100\ \%$ in some regions, and the $V_{ni}^{\Delta\text{Mu5/Mu0}}$ is $> 100\ \%$ in most regions. δq_{ised} is mainly determined by the gradient of $V_{qi}q_i$ in the vertical direction. Actually, the newly updated q_i between the substeps of the sedimentation process is used for calculating δq_{ised}. Similarly, δN_{ised} is mainly determined by the gradient of $V_{ni}N_i$ in the vertical direction. Furthermore, the ICs that fall into the clear portions of the lower model layer sublimate instantly. Therefore, both $\delta q_{ised}^{\text{Mu0}}$ and $\delta N_{ised}^{\text{Mu0}}$ are negative in most regions. This is consistent with sedimentation being a

300   sink of clouds. The δq_{ised} from the Mu2 and Mu5 experiments (i.e., $\delta q_{ised}^{\Delta\text{Mu2}}$ and $\delta q_{ised}^{\Delta\text{Mu5}}$) decrease (negative, stronger sink) in most regions mainly because of the increasing V_{qi} and higher q_i. The δN_{ised} from the Mu2 and Mu5 experiments (i.e., $\delta N_{ised}^{\Delta\text{Mu2}}$ and $\delta N_{ised}^{\Delta\text{Mu5}}$) increase (positive, weaker sink) in a few layers over the tropics. This is mainly due to the changes in the vertical gradient of N_i. Both the ΔMu2 and ΔMu5 experiments show that the changes in δq_{ised} and δN_{ised} are generally weaker than the changes in δq_{idep}, δq_{iatuo} (i.e., $q_i \times q_{iauto}/q_i$), and δN_{inuc}. In short, the fall velocities (i.e., V_{qi} and V_{ni}) and their

305   impacts on ice clouds (i.e., δq_{ised} and δN_{ised}) are mainly determined by the cloud properties (i.e., q_i, N_i, R_{qi}, and R_{qi}^*). Although the sedimentation process is also a main factor that determines the cloud properties, the changes in the sedimentation process that are caused by the increasing μ_i are not as strong as those in the deposition/sublimation, autoconversion, and nucleation processes.

    Based on the analyses presented above, it can be concluded that increasing μ_i would lead to a climate equilibrium state with

310   higher q_i and lower N_i in most regions. The changes in the statistical mean radii (i.e., R_{qi}, R_{ni}, and R_{ei}) and ice-phase cloud microphysical processes (i.e., δq_{idep}, q_{iauto}/q_i, N_{iauto}/N_i, δN_{inuc}, δq_{ised} and δN_{ised}) are mainly determined by the higher q_i, lower N_i, and increasing μ_i. On the other hand, the higher q_i and lower N_i can largely be explained by the changes in the ice-phase cloud microphysical processes (i.e., δq_{idep}, q_{iauto}/q_i, and δN_{inuc}) that are caused by the increasing μ_i. Furthermore, the ΔMu2 and ΔMu5 experiments show very similar spatial patterns for the μ_i-induced changes. This suggests that the impact of μ_i on

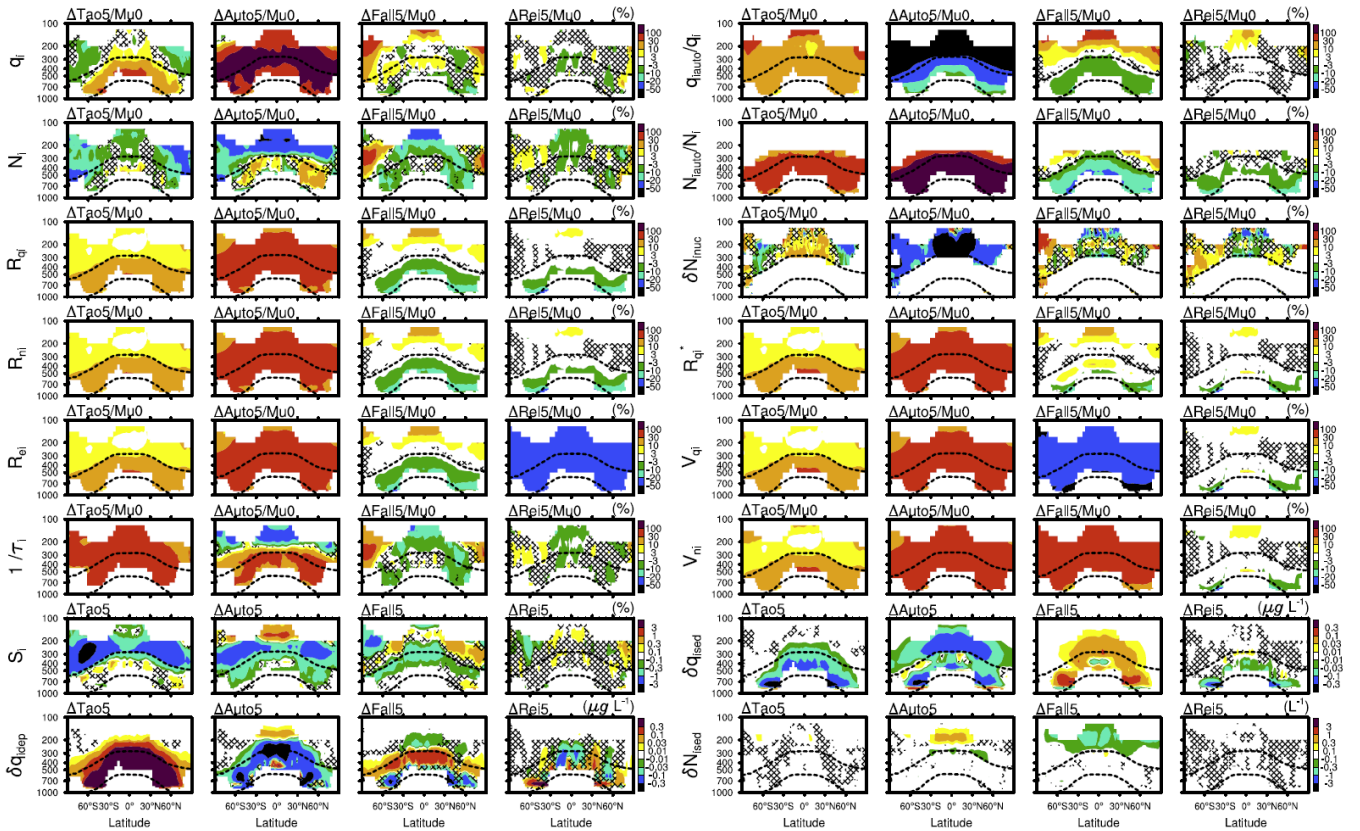315   the simulated climate equilibrium state is stable.

Figure 3. Similar to Fig. 2 but for the ΔTao5, ΔAuto5, ΔFall5 and ΔRei5 experiments. Except for the R_{ei}^{Rei5}, all statistical mean radii are calculated with $\mu_i = 0$.
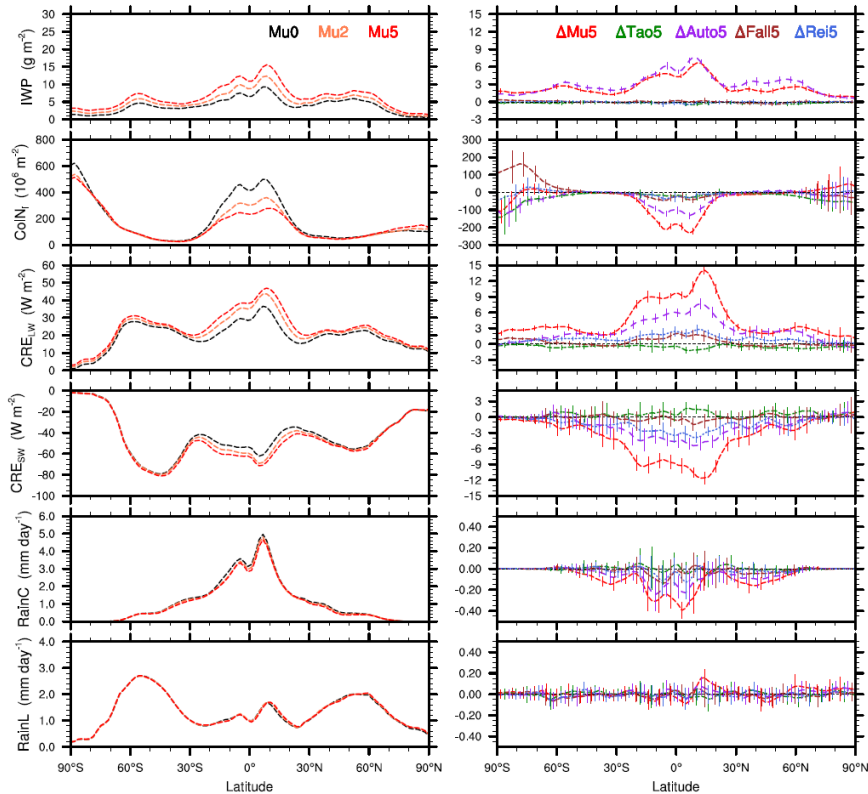
320   Fig. 3 shows the changes in the simulated climate equilibrium states that are caused by each individual μ_i-related process. The $1/\tau_i$ from the Tao5 experiment is significantly increased ($1/\tau_i^{\Delta Tao5/Mu0}$). Similar to the ΔMu2 and ΔMu5 experiments, this increasing $1/\tau_i$ could lead to a higher equilibrium state of q_i in the mixed-phase cloud layers ($q_i^{\Delta Tao5/Mu0}$) via the deposition/sublimation process ($\delta q_{idep}^{\Delta Tao5}$). However, this increasing $1/\tau_i$ leads to lower q_i and lower N_i in most of the pure ice cloud layers. The main reason might be that the ICs grow faster and their lifetimes become shorter (Mitchell, 1991;

325   DeMott et al., 2010; Storelvmo et al., 2013). The q_{iauto}/q_i from the Auto5 experiment is significantly decreased ($q_{iauto}/q_i^{\Delta Tao5/Mu0}$). This could lead to a higher q_i in nearly all regions ($q_i^{\Delta Auto5/Mu0}$) and a lower N_i in the pure ice cloud layers ($N_i^{\Delta Auto5/Mu0}$). The mechanism is the same as that introduced based on the ΔMu2 and ΔMu5 experiments. It is noteworthy that the N_i from the Auto5 experiment is slightly increased in some mixed-phase cloud layers. The main reason might be that the accretion of N_i by snow is significantly decreased in the mixed-phase cloud layers (not shown) due to the difficult

330   autoconversion process. The V_{qi} from the Fall5 experiment is significantly decreased ($V_{qi}^{\Delta Fall5/Mu0}$), and the sink term of q_i due to sedimentation becomes weaker (i.e., positive $\delta q_{ised}^{\Delta Fall5}$) in most regions. Unlike the $V_{qi}^{\Delta Fall5/Mu0}$, the V_{ni} from the Fall5 experiment obviously increase ($V_{ni}^{\Delta Fall5/Mu0}$), and the sink term of N_i due to sedimentation becomes stronger (i.e., negative

14

$\delta N_{ised}{}^{\Delta Fall5}$) in the pure ice cloud layers. These might be the main reasons for the increase in q_i and the decrease in N_i in the pure ice cloud layers over the tropics ($q_i{}^{\Delta Fall5/Mu0}$ and $N_i{}^{\Delta Fall5/Mu0}$). It is interesting to note that the R_{qi}, R_{ni}, and R_{ei} from the

335   Fall5 experiment all increase in pure ice cloud layers (i.e., upper layers) and decrease in mixed-phase cloud layers (i.e., lower layers). This can be explained by the μ_i-induced weaker size-sorting mechanism (Section 3.1). The R_{ei} from the Rei5 experiment ($R_{ei}{}^{\Delta Rei5/Mu0}$) is significantly decreased. Because the change of R_{ei} does not directly affect the cloud microphysical processes, the changes in cloud properties from the ΔRei5 experiment are not statistically significant in most regions. Taken overall, the above analyses clarify the mechanism of μ_i's impacts. Increasing μ_i in autoconversion impacts pure ice clouds the

340   most (i.e., significantly increased q_i and significantly decreased N_i in the pure ice cloud layers). Furthermore, increasing μ_i in autoconversion also leads to a much higher q_i in the mixed-phase cloud layers. Increasing μ_i in deposition/sublimation can also lead to a higher q_i in the mixed-phase cloud layers. Increasing μ_i in sedimentation can lead to a higher IC radius in the upper layers and lower IC radius in the lower layers. The impacts from sedimentation and deposition/sublimation are obviously weaker than those from autoconversion. The changes caused by increasing μ_i in the radiative process (i.e., R_{ei}) are

345   relatively chaotic.

The above analyses focus on cloud properties and cloud microphysical processes (i.e., in-cloud variables). This paragraph discusses the impacts of μ_i on radiation and precipitation. The annual zonal mean distributions of the ice water path (IWP), column N_i (ColN$_i$), longwave (CRE$_{LW}$) and shortwave (CRE$_{SW}$) cloud radiative effects, and convective (RainC) and large-scale (RainL) precipitation rates are shown in Fig. 4, and the corresponding global annual mean values are listed in Table 4.

350   The comparison of the Mu0, Mu2 and Mu5 experiments shows that the zonal mean IWPs over all latitudes clearly increase with increasing μ_i. This is consistent with the changes in in-cloud q_i (Fig. 2). The comparison of the ΔMu5, ΔTao5, ΔAuto5, ΔFall5 and ΔRei5 experiments shows that the μ_i-induced increases in IWP are mainly provided by the autoconversion process. Compared to the Mu0 experiment, the ColN$_i$ from the Mu2 and Mu5 experiments obviously decrease over tropical regions. It is clear that the autoconversion process is also the main contributor to the decreases in ColN$_i$ (Fig. 4, right

355   column). Compared to the Mu0 experiment, both CRE$_{LW}$ and CRE$_{SW}$ from the Mu2 and Mu5 experiments are obviously enhanced mainly because of the increasing IWPs. It is clear that the enhancements of CRE$_{LW}$ and CRE$_{SW}$ are also mainly contributed to by the autoconversion process (Fig. 4). Both the CRE$_{LW}$ and CRE$_{SW}$ from the Rei5 experiment are also obviously enhanced in terms of their zonal mean values (Fig. 4) and global mean values (Table 4, CRE$_{LW}{}^{\Delta Rei5}$ = 1.29 W m^{-2} and CRE$_{SW}{}^{\Delta Rei5}$ = -1.79 W m^{-2}). This suggests that the impact of μ_i on R_{ei} could lead to considerable changes in the Earth's

360   radiation budget. Compared to the impacts of μ_i on radiation, the impact on large-scale precipitation (i.e., RainL) is not statistically significant (Fig. 4, left column). However, the convective precipitation from the ΔMu5 experiment (i.e., RainC$^{\Delta Mu5}$) is significantly reduced over the tropics and subtropics (Fig. 4, right column). The reason is that the increase in ice clouds (i.e., q_i) increases atmospheric stability via the radiative budget and then leads to weaker convective precipitation (Andrews et al., 2010; Wang et al., 2014). Overall, the impacts of μ_i on radiation and precipitation are considerable. The

365   global mean CRE$_{LW}{}^{\Delta Mu5}$, CRE$_{SW}{}^{\Delta Mu5}$ and RainC$^{\Delta Mu5}$ are 5.58 W m^{-2}, -5.34 W m^{-2} and -0.12 mm day^{-1}, respectively. These changes are mainly contributed to by the autoconversion process. Furthermore, the comparisons between the ΔMu2 and

15

ΔMu5 experiments (Fig. 4 and Table 4) show that, in most cases, the μ_i-induced changes are enhanced with increasing $\Delta\mu_i$. This suggests that, in terms of the zonal mean and global mean values, the impacts of μ_i are relatively stable.

Figure 4. Annual zonal mean distributions of the ice water path (IWP), column N_i (ColN$_i$), longwave and shortwave cloud radiative effects (CRE$_{LW}$ and CRE$_{SW}$), and convective and large-scale precipitation rates (RainC and RainL). In the right panel (i.e., Δ), the vertical bars overlying these lines indicate the ranges of two standard deviations from the difference of each of 10 years at different latitudes.

Table 4. The global annual mean variables are shown in Fig. 4. The corresponding standard deviations calculated from the difference of each year for 10 years are shown in brackets.

Experiments	Mu0	ΔMu2	ΔMu5	ΔTao5	ΔAuto5	ΔFall5	ΔRei5
IWP (g m^{-2})	4.74	1.37(0.10)	2.97(0.06)	-0.20(0.05)	3.64(0.06)	-0.01(0.04)	-0.09(0.06)
ColN$_i$ (10^8 m^{-2})	1.89	-0.41(0.06)	-0.56(0.04)	-0.15(0.03)	-0.37(0.03)	-0.06(0.04)	-0.07(0.05)
CRE$_{LW}$ (W m^{-2})	22.22	3.40(0.12)	5.58(0.13)	-0.52(0.07)	3.40(0.11)	0.49(0.09)	1.29(0.10)
CRE$_{SW}$ (W m^{-2})	-49.25	-3.00(0.43)	-5.34(0.31)	0.54(0.38)	-2.52(0.46)	-0.20(0.36)	-1.79(0.24)
RainC (mm day^{-1})	1.57	-0.08(0.01)	-0.12(0.01)	0 (0.01)	-0.07(0.01)	-0.02(0.01)	-0.02(0.01)
RainL (mm day^{-1})	1.39	0.01(0.01)	0.01(0.01)	0 (0.01)	0.01(0.01)	0 (0)	0 (0.01)

16

4 Summary and conclusions

This paper investigates the impacts of μ_i on climate simulations with the CAM6 model. To achieve this, the two-moment bulk cloud microphysics scheme used in CAM6 was modified to consider the μ's impacts by a tunable parameter. After that, the impacts of μ_i on the IC size distribution and μ_i-related cloud microphysical processes are illustrated first by calculation equations and off-line tests, and the impacts of μ_i on the climate simulations are then analyzed with the CAM6 model.

380   The impacts of μ_i on the IC size distribution and various statistical mean radii are clearly explained by the calculation equations. R_{qi} can be calculated from q_i and N_i, and the normalized IC size distribution (i.e., the relative contributions from each bin) can be calculated from R_{qi} and μ_i. The impacts of μ_i on mass-weighted size distribution is obviously different from that on the commonly used number-weighted size distribution (Fig.1). Unlike the number contributions, the mass contributions of the larger size bins significantly decrease with increasing μ_i because the mass contribution is more sensitive

385   to the IC radius. In the bulk cloud microphysics scheme, the physical processes are calculated based on various statistical mean radii. The ratios of the other statistical mean radii (i.e., R_{ni}, R_{ai}, and R_{ei}) to R_{qi} are functions of μ_i. At $\mu_i \geq 0$, R_{ni} and R_{ai} are always less than R_{qi}, whereas R_{ei} is always greater than R_{qi}. The differences among these statistical mean radii become small with increasing μ_i, which is consistent with the narrower size distribution determined by higher μ_i values.

The impacts of μ_i on the μ_i-related cloud microphysical processes are clearly illustrated by the off-line tests. Under the same

390   q_i and N_i (R_{qi} is also fixed), the IC deposition/sublimation process is considerably accelerated with increasing μ_i because the R_{ni} used for calculating deposition/sublimation is increasing with increasing μ_i. Under the same R_{qi} (R_{qi} is much less than the snow radius), the autoconversion of IC to snow obviously becomes difficult with increasing μ_i because the portion of ICs with radii greater than the threshold ($> R_{cs}$) decreases under the narrow size distribution. A major effect of IC sedimentation is size-sorting because V_{qi} is greater than V_{ni}, and μ_i plays an important role in determining the rate of size-sorting (Milbrandt

395   and Yau, 2005). In this study, the off-line tests clearly show that the difference in IC radius between two adjacent model layers caused by sedimentation becomes small with increasing μ_i because the difference between V_{qi} and V_{ni} becomes small (i.e., the size-sorting rate becomes slow).

The climate simulations show that the impacts of μ_i on the ice cloud properties are notable, and the main corresponding mechanisms are clear. After increasing μ_i from 0 to 2 and 5, q_i significantly increases, while N_i significantly decreases. The

400   accelerated deposition process contributes to the higher q_i in the mixed-phase cloud layers where the ice supersaturation ($S_i >$ 0) is relatively stable. The difficult autoconversion process leads to longer IC lifetime and higher q_i. Meanwhile, N_i significantly decreases because the newly formed IC number density is significantly decreased owing to the longer IC lifetime and higher q_i. The experiments with only one modified μ_i-related process make the mechanisms of μ_i's impacts more clear. Autoconversion contributes the most. The μ_i also has considerable impacts on radiation and precipitation. After

405   increasing μ_i from 0 to 5, the global mean CRE_{LW} is increased (stronger warming effect) by 5.58 W m^{-2} (25.11 %). Meanwhile, the CRE_{SW} is decreased (less cooling effect) by -5.34 W m^{-2} (10.84 %). The enhancement of the cloud radiative effects is largely provided by the higher equilibrium state of q_i. The considerably stronger CRE_{LW} could increase the

atmospheric stability and then lead to weaker convective precipitation (Andrews et al., 2010; Wang et al., 2014). As expected, after increasing μ_i from 0 to 5, the global mean RainC is decreased by −0.12 mm day^{-1} (7.64 %). In short, the

410 impacts of μ_i on climate simulations are significant. This suggests that the μ_i (i.e., the PSD of ICs) and μ_i-related cloud microphysical processes deserve a more realistic representation in climate models, especially for cloud schemes with autoconversion. Fortunately, there have been some studies that can help to address this issue. Such as, μ_i is described by an empirical formula (Eidhammer et al., 2017), μ_i is prognosted in a three-moment cloud scheme (Milbrandt et al., 2021), and single-ice-category cloud schemes could obviate the need for autoconversion process (e.g., Morrison and Milbrandt, 2015;

415 Eidhammer et al., 2017; Zhao et al., 2017).

This study only focuses on the impacts of μ_i, the default tunable parameters (except for μ_i) are used in all the simulations. After improving the representation of μ_i-related processes, further model tuning and analyses are required based on the updated cloud scheme. Therefore, this study does not estimate which value of μ_i could lead to a better simulation. Finally, it is necessary to point out that the main mechanism for μ_i's impacts introduced in this study (i.e., autoconversion becomes

420 difficult with increasing μ_i) is not applicable to climate simulations with the single-ice-category cloud scheme. However, similar to the μ_i's impact on autoconversion, the interaction between small ICs and large ICs (e.g., the accretion of small ICs by large ICs) should become weaker with increasing μ_i (i.e., narrower size distribution). Therefore, we can speculate that the impacts of μ_i on climate simulations with the single-ice-category cloud scheme may still be worth noting.

Appendix A: The limitation in the use of gamma functions for representing ice-phase PSDs in bulk cloud
425 **microphysics schemes**

Here, we show the PSDs represented by gamma functions of the form $N'(D) = N_0 D^\mu e^{-\lambda D}$ firstly, and then discuss the reason why bulk cloud microphysics schemes usually constrain μ to be nonnegative.

Fig. A1 shows that the PSDs are relatively wide with negative μ. Under negative μ, the particle number densities (N') are increased with decreasing D, and become very huge at $D < 1$ μm (Fig. A1 left). In the real world, the cloud particles are

430 usually not less than 1 μm. It is necessary to point out that the contribution from small particles (e.g., $D < 50$ μm) is usually neglected for getting the gamma-fitted PSD from observations (Heymsfield, 2003). For instance, when only considering the particles over sizes (D) from as small as 10 μm to as large as 2000 μm (measured particle size), the uncertainty from the extrapolation below 50 μm is negligible in the linear space of particle size (Fig. A1 right). Therefore, some gamma-fitted PSDs from observations might show negative μ values (e.g., Heymsfield, 2003; Heymsfield et al., 2013; Schmitt and
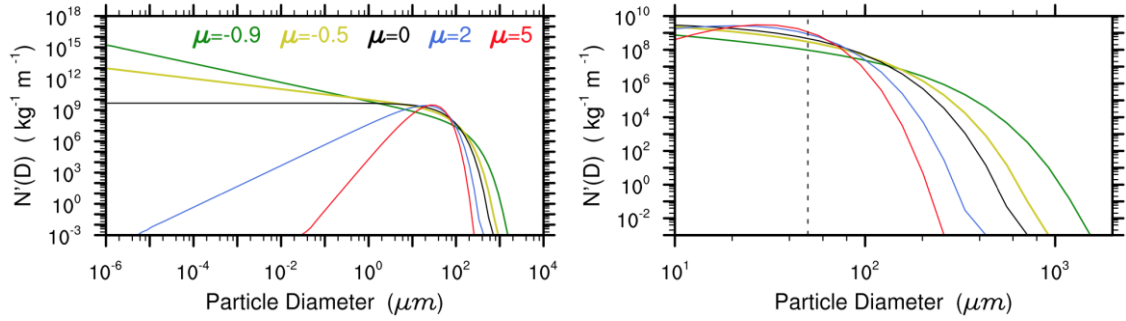
435 Heymsfield, 2009).

Figure A1. The particle number densities (N', which is a function of D) calculated from the gamma distributions with various μ values. Here, the total particle number and mass-weighted diameter are set to 10^5 kg^{-1} ($\sim$50 L^{-1}) and 40 μm, respectively. Note different markers in the Y-Axis and X-Axis between the left column and right column. The vertical black line indicates $D = 50$ μm.

440   Unlike the gamma-fitted PSDs from observations (small particles might be neglected), the gamma functions used in bulk cloud microphysics schemes represent the particles with diameter from 0 to ∞ (hereafter, mathematical size range). For instance, the other two gamma distribution parameters (N_0 and λ) used in the bulk cloud scheme are calculated by the particle's mass (q) and number (N), and some μ's gamma functions ($\lambda = [\frac{\pi \rho}{6} \frac{N}{q} \frac{\Gamma(4+\mu)}{\Gamma(1+\mu)}]^{1/3}$, $N_0 = \frac{N\lambda^{(1+\mu)}}{\Gamma(1+\mu)}$). Because the gamma function, $\Gamma(x) = \int_0^\infty t^{x-1}e^{-t}\,dt$, is used for derivating these calculation formulas, the q and N in these calculation formulas

445   indicate the mass and number of particles from the mathematical size range (i.e., 0 to ∞). Furthermore, the μ must be greater than -1 in these two calculation formulas because the negative integer and zero are the singularity of the gamma function. Under negative μ ($-1 < \mu < 0$, the N' is very huge at $D < 1$ μm, Fig. A1 left), more attention should be paid to using the gamma function because it integrates from 0 to ∞. Fig. A2 shows the relative number contributions from each radius bin of ICs under different R_{qi}. Table A1 lists the contributions of ICs with a radius from 1 μm to 1000 μm (hereafter, realistic size

450   range) to the total number (i.e., the N_i from the mathematical size range). At $\mu_i \geq 0$ (i.e., $\mu_i = 0$, 2, and 5), the number contributions are mostly from the realistic size range except for one case ($\mu_i = 0$ and $R_{qi} = 5$ μm). Under the small ICs scenario (i.e., $R_{qi} = 5$ μm) and $\mu_i = -0.5$, the number of ICs from the realistic size range only contributes $\sim$1/2 to the total number. At $\mu_i = -0.9$, the contributions of ICs from the realistic size range cannot reach 1/2 even for the large ICs scenario (i.e., $R_{qi} = 60$ μm). In other words, under negative μ_i, the gamma distribution functions (mathematical size range) used in the

455   bulk cloud schemes might be not suited for representing realistic ICs (realistic size range). Therefore, our study only evaluates the impacts of changing μ_i from 0 to 2, 5.
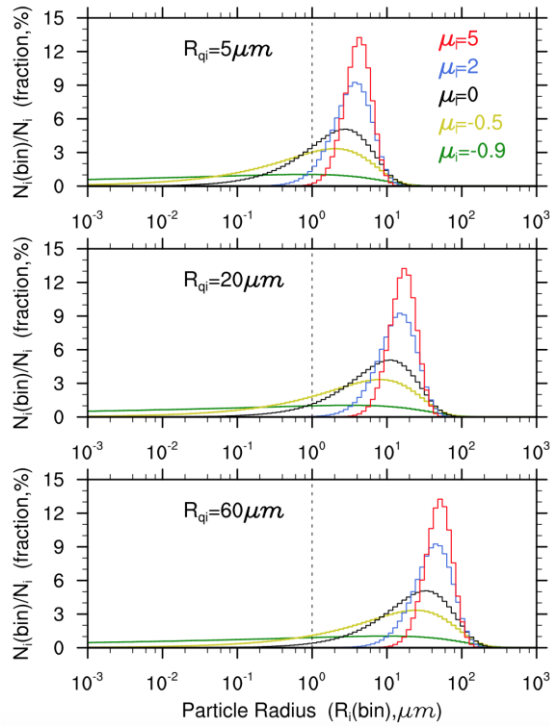
Figure A2. The relative number contributions from each radius bin of ICs under different R_{qi}. A total of 100 bins were used here. Each bin width is the same based on the logarithm of the particle radius.

460   **Table A1.** The contributions of ICs from the realistic size range (i.e., 1~1000 μm) to the total number.

	$\mu_i = -0.9$	$\mu_i = -0.5$	$\mu_i = 0$	$\mu_i = 2$	$\mu_i = 5$
$R_{qi} = 5$ μm	17 %	51 %	73 %	97 %	100 %
$R_{qi} = 20$ μm	27 %	74 %	92 %	100 %	100 %
$R_{qi} = 60$ μm	34 %	85 %	97 %	100 %	100 %

*The PSDs of ICs are represented by gamma functions with a range from 0 to ∞. The contributions given are only approximate because the value of the incomplete gamma function is not very accurate.

Code and data availability

The CAM6 model used in this study is the atmospheric component of the Community Earth System Model version 2.1.3
465   (CESM2.1.3). The CESM2.1.3 is a release version of CESM2. The model code, scripts, and input data are freely available through a public GitHub repository (https://escomp.github.io/CESM/versions/cesm2.1/html/downloading_cesm.html; last access: 9 May 2022). More details about model workflow can be found in the corresponding quick-start guide. The modified model code, model run control scripts, and simulation results postprocessing scripts covering every data processing action for all the model results reported in the paper are available online at DOI: 10.5281/zenodo.6409156. The FORTRAN code

470   for offline tests is also archived with the same DOI. Furthermore, the NCL scripts and data for making every figure are also available at the above DOI.

Competing interests

The authors declare that they have no conflict of interest.

Author contribution

475   XS designed this study. WZ and XS designed the CAM6 model experiments and developed the modified model code. XS and WZ analyzed the results and wrote the original paper. All authors contributed to improving and reviewing the manuscript.

Acknowledgments

References

Andrews, T., Forster, P. M., Boucher, O., Bellouin, N., and Jones, A.: Precipitation, radiative forcing and global temperature
485   change, Geophysical Research Letters, 37, L14701, https://doi.org/10.1029/2010GL043991, 2010.

Barahona, D., Molod, A., Bacmeister, J., Nenes, A., Gettelman, A., Morrison, H., Phillips, V., and Eichmann, A.: Development of two-moment cloud microphysics for liquid and ice within the NASA Goddard Earth Observing System Model (GEOS-5), Geosci. Model Dev., 7, 1733-1766, https://doi.org/10.5194/gmd-7-1733-2014, 2014.

Bogenschutz, P. A., Gettelman, A., Morrison, H., Larson, V. E., Craig, C., and Schanen, D. P.: Higher-order turbulence
490   closure and its impact on climate simulations in the Community Atmosphere Model, Journal of Climate, 26, 9655-9676, https://doi.org/10.1175/jcli-d-13-00075.1, 2013.

Bogenschutz, P. A., Gettelman, A., Hannay, C., Larson, V. E., Neale, R. B., Craig, C., and Chen, C.-C.: The path to CAM6: coupled simulations with CAM5.4 and CAM5.5, Geoscientific Model Development, 11, 235–255, https://doi.org/10.5194/gmd-11-235-2018, 2018.

495　Bony, S., Stevens, B., Frierson, D. M. W., Jakob, C., Kageyama, M., Pincus, R., Shepherd, T. G., Sherwood, S. C., Siebesma, A. P., Sobel, A. H., Watanabe, M., and Webb, M. J.: Clouds, circulation and climate sensitivity, Nature Geoscience, 8, 261-268, https://doi.org/10.1038/ngeo2398, 2015.

Danabasoglu, G., Lamarque, J.-F., Bacmeister, J., Bailey, D. A., DuVivier, A. K., Edwards, J., Emmons, L. K., Fasullo, J., Garcia, R., Gettelman, A., Hannay, C., Holland, M. M., Large, W. G., Lauritzen, P. H., Lawrence, D. M., Lenaerts, J. T. M.,

500　Lindsay, K., Lipscomb, W. H., Mills, M. J., Neale, R., Oleson, K. W., Otto-Bliesner, B., Phillips, A. S., Sacks, W., Tilmes, S., van Kampenhout, L., Vertenstein, M., Bertini, A., Dennis, J., Deser, C., Fischer, C., Fox-Kemper, B., Kay, J. E., Kinnison, D., Kushner, P. J., Larson, V. E., Long, M. C., Mickelson, S., Moore, J. K., Nienhouse, E., Polvani, L., Rasch, P. J., and Strand, W. G.: The community earth system model version 2 (CESM2), Journal of Advances in Modeling Earth Systems, 12, e2019MS001916, https://doi.org/10.1029/2019MS001916, 2020.

505　DeMott, P. J., Prenni, A. J., Liu, X., Kreidenweis, S. M., Petters, M. D., Twohy, C. H., Richardson, M. S., Eidhammer, T., and Rogers, D. C.: Predicting global atmospheric ice nuclei distributions and their impacts on climate, P. Natl. Acad. Sci. USA, 107, 11217–11222, https://doi.org/10.1073/pnas.0910818107, 2010.

Eidhammer, T., Morrison, H., Bansemer, A., Gettelman, A., and Heymsfield, A. J.: Comparison of ice cloud properties simulated by the Community Atmosphere Model (CAM5) with in-situ observations, Atmospheric Chemistry and Physics, 14,

510　10103-10118, https://doi.org/10.5194/acp-14-10103-2014, 2014.

Eidhammer, T., Morrison, H., Mitchell, D., Gettelman, A., and Erfani, E.: Improvements in global climate model microphysics using a consistent representation of ice particle properties, Journal of Climate, 30, 609-629, https://doi.org/10.1175/jcli-d-16-0050.1, 2017.

Erfani, E. and Mitchell, D. L.: Developing and bounding ice particle mass- and area-dimension expressions for use in

515　atmospheric models and remote sensing, Atmospheric Chemistry and Physics, 16, 4379-4400, https://doi.org/10.5194/acp-16-4379-2016, 2016.

Gettelman, A. and Morrison, H.: Advanced two-moment bulk microphysics for global models. Part I: Off-line tests and comparison with other schemes, Journal of Climate, 28, 1268-1287, https://doi.org/10.1175/jcli-d-14-00102.1, 2015.

Heymsfield, A. J.: Properties of tropical and midlatitude ice cloud particle ensembles. Part II: Applications for mesoscale

520　and climate models, Journal of the Atmospheric Sciences, 60, 2592-2611, https://doi.org/10.1175/1520-0469(2003)060<2592:Potami>2.0.Co;2, 2003.

Heymsfield, A. J., Schmitt, C., and Bansemer, A.: Ice cloud particle size distributions and pressure-dependent terminal velocities from in situ observations at temperatures from 0 to −86 ∘C, J. Atmospheric Sciences, 70, 4123–4154, https://doi.org/10.1175/JAS-D-12-0124.1, 2013.

525　Khain, A. P., Beheng, K. D., Heymsfield, A., Korolev, A., Krichak, S. O., Levin, Z., Pinsky, M., Phillips, V., Prabhakaran, T., Teller, A., van den Heever, S. C., and Yano, J. I.: Representation of microphysical processes in cloud-resolving models: Spectral (bin) microphysics versus bulk parameterization, Reviews of Geophysics, 53, 247-322, https://doi.org/10.1002/2014rg000468, 2015.

King, A. D., Lane, T. P., Henley, B. J., and Brown, J. R.: Global and regional impacts differ between transient and equilibrium warmer worlds, Nature Climate Change, 10, 42-47, https://doi.org/10.1038/s41558-019-0658-7, 2020.

Korolev, A. V. and Mazin, I. P.: Supersaturation of water vapor in clouds, Journal of the Atmospheric Sciences, 60, 2957-2974, https://doi.org/10.1175/1520-0469(2003)060<2957:Sowvic>2.0.Co;2, 2003.

Krämer, M., Schiller, C., Afchine, A., Bauer, R., Gensch, I., Mangold, A., Schlicht, S., Spelten, N., Sitnikov, N., Borrmann, S., de Reus, M., and Spichtinger, P.: Ice supersaturations and cirrus cloud crystal numbers, Atmos. Chem. Phys., 9, 3505-3522, https://doi.org/10.5194/acp-9-3505-2009, 2009.

Larson, V. E.: CLUBB-SILHS: A parameterization of subgrid variability in the atmosphere, arXiv preprint arXiv:1711.03675, 2017.

Li, J. L. F.: An observationally based evaluation of cloud ice water in CMIP3 and CMIP5 GCMsand contemporary reanalyses using contemporary satellite data, J Geophys Res, 117, https://doi.org/10.1029/2012JD017640, 2012.

Liou, K.: Influence of cirrus clouds on weather and climate processes: A Global Perspective, Monthly Weather Review, 114, 1167-1199, https://doi.org/10.1175/1520-0493(1986)114<1167:IOCCOW>2.0.CO;2, 1986.

Liu, X. H. and Penner, J. E.: Ice nucleation parameterization for global models, Meteorologische Zeitschrift, 14, 499-514, https://doi.org/10.1127/0941-2948/2005/0059, 2005.

Loftus, A. M., Cotton, W. R., and Carrió, G. G.: A triple-moment hail bulk microphysics scheme. Part I: Description and initial evaluation, Atmospheric Research, 149, 35-57, https://doi.org/10.1016/j.atmosres.2014.05.013, 2014.

Lohmann, U., Stier, P., Hoose, C., Ferrachat, S., Kloster, S., Roeckner, E., and Zhang, J.: Cloud microphysics and aerosol indirect effects in the global climate model ECHAM5-HAM, Atmos. Chem. Phys., 7, 3425-3446, https://doi.org/10.5194/acp-7-3425-2007, 2007.

Luo, Z. and Rossow, W. B.: Characterizing tropical cirrus life cycle, evolution, and interaction with upper-tropospheric water vapor using Lagrangian trajectory analysis of satellite observations, Journal of Climate, 17, 4541-4563, https://doi.org/10.1175/3222.1, 2004.

McFarquhar, G. M., Hsieh, T.-L., Freer, M., Mascio, J., and Jewett, B. F.: The characterization of ice hydrometeor gamma size distributions as volumes in $N0–\lambda–\mu$ phase space: Implications for microphysical process modeling, Journal of the Atmospheric Sciences, 72, 892-909, https://doi.org/10.1175/jas-d-14-0011.1, 2015.

Milbrandt, J. A. and McTaggart-Cowan, R.: Sedimentation-induced errors in bulk microphysics schemes, Journal of the Atmospheric Sciences, 67, 3931-3948, https://doi.org/10.1175/2010jas3541.1, 2010.

Milbrandt, J. A. and Yau, M. K.: A multimoment bulk microphysics parameterization. Part I: Analysis of the role of the spectral shape parameter, Journal of the Atmospheric Sciences, 62, 3051-3064, https://doi.org/10.1175/jas3534.1, 2005.

Milbrandt, J. A., Morrison, H., Dawson II, D. T., and Paukert, M.: A triple-moment representation of ice in the Predicted Particle Properties (P3) microphysics scheme, Journal of the Atmospheric Sciences, 78, 439-458, https://doi.org/10.1175/jas-d-20-0084.1, 2021.

Mitchell, D. L.: Evolution of Snow-Size Spectra in Cyclonic Storms. Part II: Deviations from the Exponential Form, J. Atmos. Sci., 48, 1885–1899, https://doi.org/10.1175/1520-0469(1991)048<1885:EOSSSI>2.0.CO;2, 1991.Mitchell, D. L., Rasch, P., Ivanova, D., McFarquhar, G., and Nousiainen, T.: Impact of small ice crystal assumptions on ice sedimentation rates in cirrus clouds and GCM simulations, Geophys. Res. Lett., 35, L09806, https://doi.org/10.1029/2008gl033552, 2008.

Morrison, H. and Gettelman, A.: A new two-moment bulk stratiform cloud microphysics scheme in the community atmosphere model, version 3 (CAM3). Part I: Description and numerical tests, Journal of Climate, 21, 3642-3659, https://doi.org/ 10.1175/2008jcli2105.1, 2008.

Morrison, H. and Milbrandt, J. A.: Parameterization of cloud microphysics based on the prediction of bulk ice particle properties. Part I: Scheme description and idealized tests, Journal of the Atmospheric Sciences, 72, 287-311, https://doi.org/10.1175/jas-d-14-0065.1, 2015.

Morrison, H., Curry, J. A., and Khvorostyanov, V. I.: A new double-moment microphysics parameterization for application in cloud and climate models. Part I: Description, Journal of the Atmospheric Sciences, 62, 1665-1677, https://doi.org/10.1175/jas3446.1, 2005.

Morrison, H., van Lier-Walqui, M., Fridlind, A. M., Grabowski, W. W., Harrington, J. Y., Hoose, C., Korolev, A., Kumjian, M. R., Milbrandt, J. A., Pawlowska, H., Posselt, D. J., Prat, O. P., Reimel, K. J., Shima, S.-I., van Diedenhoven, B., and Xue, L.: Confronting the challenge of modeling cloud and precipitation microphysics, Journal of Advances in Modeling Earth Systems, 12, e2019MS001689, https://doi.org/10.1029/2019MS001689, 2020.

Paukert, M., Fan, J., Rasch, P. J., Morrison, H., Milbrandt, J. A., Shpund, J., and Khain, A.: Three-moment representation of rain in a bulk microphysics model, Journal of Advances in Modeling Earth Systems, 11, 257-277, https://doi.org/10.1029/2018MS001512, 2019.

Proske, U., Ferrachat, S., Neubauer, D., Staab, M., and Lohmann, U.: Assessing the potential for simplification in global climate model cloud microphysics, Atmos. Chem. Phys. Discuss., 2021, 1-40, https://doi.org/10.5194/acp-2021-801, 2021.

Salzmann, M., Ming, Y., Golaz, J. C., Ginoux, P. A., Morrison, H., Gettelman, A., Krämer, M., and Donner, L. J.: Two-moment bulk stratiform cloud microphysics in the GFDL AM3 GCM: description, evaluation, and sensitivity tests, Atmos. Chem. Phys., 10, 8037-8064, https://doi.org/10.5194/acp-10-8037-2010, 2010.

Schmitt, C. G., and Heymsfield, A. J.: The size distribution and mass-weighted terminal velocity of low-latitude tropopause cirrus crystal populations, Journal of the Atmospheric Sciences, 66, 2013–2028, https://doi.org/10.1175/2009JAS3004.1, 2009.

Schumann, U., Mayer, B., Gierens, K., Unterstrasser, S., Jessberger, P., Petzold, A., Voigt, C., and Gayet, J.-F.: Effective radius of ice particles in cirrus and contrails, Journal of the Atmospheric Sciences, 68, 300-321, https://doi.org/10.1175/2010jas3562.1, 2011.

Sherwood, S. C., Bony, S., Boucher, O., Bretherton, C., Forster, P. M., Gregory, J. M., and Stevens, B.: Adjustments in the forcing-feedback framework for understanding climate change, Bulletin of the American Meteorological Society, 96, 217-228, https://doi.org/10.1175/bams-d-13-00167.1, 2015.

Shi, X., Liu, X., and Zhang, K.: Effects of pre-existing ice crystals on cirrus clouds and comparison between different ice nucleation parameterizations with the Community Atmosphere Model (CAM5), Atmospheric Chemistry and Physics, 15, 1503-1520, https://doi.org/10.5194/acp-15-1503-2015, 2015.

Spichtinger, P. and Gierens, K. M.: Modelling of cirrus clouds – Part 1a: Model description and validation, Atmos. Chem.
600   Phys., 9, 685-706, https://doi.org/10.5194/acp-9-685-2009, 2009.

Storelvmo, T., Kristjansson, J. E., Muri, H., Pfeffer, M., Barahona, D., and Nenes, A.: Cirrus cloud seeding has potential to cool climate, Geophys. Res. Lett., 40, 178–182, https://doi.org/10.1029/2012GL054201, 2013.

Wang, M. and Penner, J. E.: Cirrus clouds in a global climate model with a statistical cirrus cloud scheme, Atmos. Chem. Phys., 10, 5449-5474, https://doi.org/10.5194/acp-10-5449-2010, 2010.

605   Wang, M., Liu, X., Zhang, K., and Comstock, J. M.: Aerosol effects on cirrus through ice nucleation in the Community Atmosphere Model CAM5 with a statistical cirrus scheme, Journal of Advances in Modeling Earth Systems, 6, 756-776, https://doi.org/10.1002/2014MS000339, 2014.

Wyser, K.: The effective radius in ice clouds, Journal of Climate, 11, 1793-1802, https://doi.org/10.1175/1520-0442(1998)011<1793:Teriic>2.0.Co;2, 1998.

610   Zhang, G. J. and McFarlane, N. A.: Sensitivity of climate simulations to the parameterization of cumulus convection in the Canadian climate centre general circulation model, Atmosphere-Ocean, 33, 407-446, https://doi.org/10.1080/07055900.1995.9649539, 1995.

Zhang, G. J., Kiehl, J. T., and Rasch, P. J.: Response of climate simulation to a new convective parameterization in the National Center for Atmospheric Research Community Climate Model (CCM3), Journal of Climate, 11, 2097-2115,
615   https://doi.org/10.1175/1520-0442(1998)011<2097:Rocsta>2.0.Co;2, 1998.

Zhao, X., Lin, Y., Peng, Y., Wang, B., Morrison, H., and Gettelman, A.: A single ice approach using varying ice particle properties in global climate model microphysics, Journal of Advances in Modeling Earth Systems, 9, 2138-2157, https://doi.org/10.1002/2017MS000952, 2017.

Zhou, C., Zelinka, M. D., and Klein, S. A.: Impact of decadal cloud variations on the Earth/'s energy budget, Nature Geosci,
620   9, 871-874, https://doi.org/10.1038/ngeo2828, 2016.